Evaluating the Efficacy of Bilinear Hyperspectral Unmixing For Satellite Derived Bathymetry in Optically Shallow Waters

Forrest Corcoran*
Department of Civil and Environmental Engineering
Oregon State University
corcoraf@oregonstate.edu

Abstract

Bathymetric surveying is an important undertaking in the fields of oceanography, coastal engineering, and marine ecology. However, due to the high costs and safety risks associated with operating surveying ships in shallow waters, along with the logistic difficulties of conducting surveys in remote locations, nearshore gaps in global bathymetry datasets are common. For these reasons, there has been significant interest in developing techniques and algorithms to extract accurate bathymetric measurements from remotely sensed satellite data. In this paper, we explore a new and novel approach to extracting Satellite Derived Bathymetry (SDB) from hyperspectral imagery using a Generalized Bilinear Model (GBM) for hyperspectral unmixing. The algorithm used to conduct this experiment is based on the work of [1]. We evaluate the efficacy of this approach using data from a bathymetric lidar survey.

1 Introduction

Bathymetric surveying (i.e. topographic mapping of the seafloor) is an important undertaking for many scientific and engineering disciplines such as oceanography, coastal engineering, and marine ecology. In particular, nearshore bathymetry datasets are often used for maritime navigation, flood inundation modeling, benthic habitat modeling, and many other important endeavours. Additionally, due to the effects of tides, currents, and storm surges, nearshore bathymetry is highly dynamic relative to deeper water or dry land topography. Therefore, it is important to maintain updated bathymetric maps of nearshore areas.

Currently, the most common method for conducting bathymetric surveys is through single or multi-beam echo sounders (i.e. sonar) mounted on survey ships. These types of surveys are highly accurate and reliable, however, due to the danger and high costs associated with operating a research vessel in shallow waters, these surveys often avoid measuring nearshore areas. This has resulted in a noticeable gap in global bathymetry datasets around the worlds coasts, known as the "white ribbon".

Recently, remote sensing has gained popularity as a method for filling the nearshore bathymetric data gap. In particular, airborne bathymetric lidar has been shown to produce accurate, high resolution measurements for nearshore areas. However, while these surveys are safe and highly accurate, they are still costly and can be difficult to carry out in some remote locations. For this reason, there has been significant interest in developing techniques and algorithms to extract bathymetric measurements from extensive, regularly collected, and widely available datasets such as satellite imagery. Most of these Satellite Derived Bathymetry (SDB) techniques, such as the popular Stumpf's Ratio of Logs algorithm [4], rely on principles of radiative transfer to infer depth by comparing the reflectance of

*Ph.D. Student

Preprint. Under review.

light at different wavelengths in optically shallow water. While these techniques can be quite accurate and are widely used in the literature, they are also prone to errors due to unaccounted for optical properties such as water turbidity, suspended sediment, chlorophyll, or colored dissolved organic matter (CDOM).

In this paper, we explore a new, novel approach for measuring SDB from hyperspectral imagery. This technique, based on the work of [1], uses a generalized bilinear mixing model to estimate the abundance of different materials throughout the scene. This bilinear model takes into account second order photon interactions (i.e. photons that reflect off two endmembers before being detected by the spectrometer). We attempt to extract relative bathymetry by estimating the strength of the second order interactions between water and seafloor material. Finally, we evaluate the efficacy of this technique by comparing our results with a bathymetric lidar survey.

2 Bilinear Unmixing

It is well established that seafloor reflectance is a function of both water depth and turbidity. In fact, under mild conditions, the radiative transfer of downwelling irradiance can be effectively model via the Beer-Lambert Law, which is shown in Equation 1.

$$E_\lambda^{(z)} = E_\lambda^{(0)} e^{-K_{d_\lambda} z} \tag{1}$$

Where $E_\lambda^{(z)}$ is the downwelling irradiance of wavelength λ at depth z and K_{d_λ} is the diffuse attenuation coefficient at wavelength λ, and apparent optical property (AOP) of water that represents turbidity. The Beer-Lambert Law is of significance for this project because it shows the relationship between depth, turbidity, and measured spectral intensity of the seafloor from a remote sensing platform.

Spectral unmixing is an active area of research in remote sensing and optimization that seeks to represent each pixel in a hyperspectral or multispectral image as a weighted combination of endmember materials. This task is often accomplished using the linear mixing model (LMM), where each pixel is considered to be a linear combination of endmembers, with each endmember's coefficient representing the abundance of that material in the pixel, plus some additive noise. The LMM formulation is shown in Equation 2.

$$\mathbf{y} = \sum_{i=1}^{N} a_i \mathbf{e}_i + \mathbf{n} \tag{2}$$

Where $\mathbf{y} \in \mathbb{R}^D$ is the observed spectra at a given pixel, $\mathbf{e}_i \in \mathbb{R}^D$ is the spectrum of endmember i, a_i is the relative abundance of endmember i, and $\mathbf{n} \in \mathbb{R}^D$ is noise, with D representing the number of spectral channels and N the number of endmembers.

This formulation can be extended to matrix notation as shown in Equation 3.

$$\mathbf{Y} = \mathbf{E}\mathbf{A} + \mathbf{N} \tag{3}$$

Where $\mathbf{Y} \in \mathbb{R}^{D \times P}$ is the matrix representation of the hyperspectral image, with P representing the number of pixels, $\mathbf{A} \in \mathbb{R}^{N \times P}$ is the matrix of pixel abundances for each endmember, $\mathbf{E} \in \mathbb{R}^{D \times N}$ is the spectral dictionary of endmembers, and $\mathbf{N} \in \mathbb{R}^{D \times P}$ is the noise matrix.

While the LMM has received significant attention for its effectiveness and simplicity, it assumes that solar photons reflect off a single material between being detected by the spectrometer. While this assumption is valid in most scenarios, for regions with vertically layered surfaces such as sparse forest canopy and some urban settings, photons will commonly interact with multiple materials before being detected by the spectrometer. This is also the case for optically shallow water, where photons reflecting off the seafloor will also interact with the watercolumn, as shown in Figure 1.

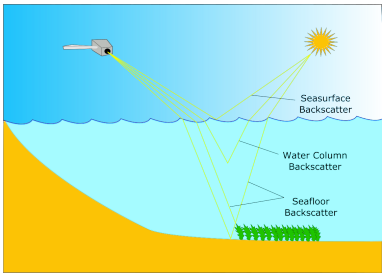

Figure 1: Schematic of the bilinear interaction between water and seafloor.

In order to incorporate the second order photon interactions into the unmixing model, we used the Generalized Bilinear Mixing Model (GBMM), which is shown in Equation 4.

$$\mathbf{y} = \sum_{i=1}^{N} a_i \mathbf{e}_i + \sum_{i=1}^{N-1} \sum_{j=i+1}^{N} b_{i,j} \mathbf{e}_i \odot \mathbf{e}_j + \mathbf{n} \tag{4}$$

Where $b_{i,j}$ represents the strength of the interaction between endmembers i and j, and $\odot$ is the Hadamard (i.e. element-wise) product. By letting $b_{i,j} = \gamma_{i,j} a_i a_j$ we can reformulate the GBMM as shown in Equation 5.

$$\mathbf{Y} = \mathbf{EA} + \mathbf{FB} + \mathbf{N} \tag{5}$$

Where $F = [\mathbf{e}_1 \odot \mathbf{e}_2, ..., \mathbf{e}_{N-1} \odot \mathbf{e}_N] \in \mathbb{R}^{D \times \frac{N(N-1)}{2}}$ and $\mathbf{B} = [\gamma_{1,2} a_1 a_2, ..., \gamma_{N-1,N} a_{N-1} a_N] \in \mathbb{R}^{\frac{N(N-1)}{2} \times P}$.

Solving the GBMM is equivalent to solving a convex optimization problem of the form shown in Equation 6.

$$\begin{aligned} \min_{\mathbf{A},\mathbf{B}} \; & \|\mathbf{Y} - \mathbf{EA} - \mathbf{FB}\|_F^2 \\ \text{subject to} \quad & \mathbf{A} \succeq 0 \\ & \mathbf{0} \preceq \mathbf{B} \preceq \mathbf{C} \end{aligned} \tag{6}$$

Where $\mathbf{C}_{(i,j),k} = \mathbf{A}_{i,k} A_{j,k}$ for $k = 1, ..., P$ and $\| \cdot \|_F$ is the Frobenius norm.

NU-BGBM Algorithm

In order to solve the optimization problem posed in Equation 6, [1] proposed the Nonlinear Unmixing Bandwise General Bilinear Model (NU-BGBM) algorithm. This model differs from the traditional GBM in that it considers the noise matrix $\mathbf{N}$ to be a combination of dense, additive, Gaussian noise, represented by a diagonal matrix $\mathbf{W} \in \mathbb{R}^{D \times D}$, where $\mathbf{W}_{i,i} = \frac{1}{\sigma_i^2}$ with σ_i^2 the variance of the noise in spectral band i, as well as spatially sparse noise, often referred to as "artifacts", represented by $\mathbf{S} \in \mathbb{R}^{D \times P}$. The new formulation is shown in Equation 7.

$$\begin{aligned} \min_{\mathbf{A},\mathbf{B},\mathbf{S}} \; & \frac{1}{2} \|\mathbf{W}(\mathbf{Y} - \mathbf{EA} - \mathbf{FB} - \mathbf{S})\|_F^2 + \lambda \|\mathbf{S}\|_1 \\ \text{subject to} \quad & \mathbf{A} \succeq 0 \\ & \mathbf{0} \preceq \mathbf{B} \preceq \mathbf{C} \end{aligned} \tag{7}$$

In order to apply the Alternating Direction Method of Multipliers (ADMM) algorithm, the problem is further reformulated, as shown in Equation 8.

$$\begin{aligned} \min_{\mathbf{A},\mathbf{B},\mathbf{S},\mathbf{V}_1,\mathbf{V}_2,\mathbf{V}_3} \; & \frac{1}{2} \|\mathbf{W}(\mathbf{Y} - \mathbf{EA} - \mathbf{FB} - \mathbf{V}_1)\|_F^2 + \mathcal{I}_{\mathbb{R}_+}(\mathbf{V}_2) + \mathcal{I}_{\mathbb{R}_\mathbf{C}}(\mathbf{V}_3) + \lambda \|\mathbf{S}\|_1 \\ \text{subject to} \quad & \mathbf{V}_1 = \mathbf{S} \\ & \mathbf{V}_2 = \mathbf{A} \\ & \mathbf{V}_3 = \mathbf{B} \end{aligned} \tag{8}$$

Where $\mathcal{I}_{\mathbb{R}_+}$ is the element-wise indicator function for the nonnegative orthant and $\mathcal{I}_{\mathbb{R}_\mathbf{C}}$ is the element-wise indicator for the interval $[\mathbf{0}, \mathbf{C}]$.

Finally, we can put the problem in its compact ADMM form, as shown by Equation 9.

$$\begin{aligned} &\min_{\mathbf{V},\mathbf{G}} g(\mathbf{V},\mathbf{G}) \\ &\text{subject to} \\ &\mathbf{GQ}+\mathbf{HV}=\mathbf{Z} \end{aligned} \tag{9}$$

where $g(\mathbf{V},\mathbf{G}) = \frac{1}{2}\|\mathbf{W}(\mathbf{Y}-\mathbf{EA}-\mathbf{FB}-\mathbf{V}_1)\|_F^2+\mathcal{I}_{\mathbb{R}_+}(\mathbf{V}_2)+\mathcal{I}_{\mathbb{R}_\mathbf{C}}(\mathbf{V}_3)+\lambda\|\mathbf{S}\|_1$, $\mathbf{G} = \begin{bmatrix}\mathbf{I} & \mathbf{0} & \mathbf{0}\\ \mathbf{0} & \mathbf{I} & \mathbf{0}\\ \mathbf{0} & \mathbf{0} & \mathbf{I}\end{bmatrix}$, $\mathbf{Q} = \begin{bmatrix}\mathbf{S}\\ \mathbf{A}\\ \mathbf{B}\end{bmatrix}$, $\mathbf{H} = \begin{bmatrix}-\mathbf{I} & \mathbf{0} & \mathbf{0}\\ \mathbf{0} & -\mathbf{I} & \mathbf{0}\\ \mathbf{0} & \mathbf{0} & -\mathbf{I}\end{bmatrix}$, $\mathbf{V} = \begin{bmatrix}\mathbf{V}_1\\ \mathbf{V}_2\\ \mathbf{V}_3\end{bmatrix}$, $\mathbf{Z} = \begin{bmatrix}\mathbf{0}\\ \mathbf{0}\\ \mathbf{0}\end{bmatrix}$.

Using this form, we can write the augmented Lagrangian, as shown in Equation 10, as well as the primal and dual residuals, shown in Equations 11 and 12, respectively.

$$\mathcal{L}(\mathbf{V},\mathbf{G},\Lambda) = g(\mathbf{V},\mathbf{G}) + \frac{\mu}{2}\|\mathbf{GQ}+\mathbf{HV}-\mathbf{Z}-\Lambda\|_F^2 \tag{10}$$

$$r^{k+1} = \mathbf{GQ}^{k+1}+\mathbf{HV}^{k+1} \tag{11}$$

$$d^{k+1} = \mu\mathbf{G^T H}(\mathbf{Q}^{k+1}-\mathbf{Q}^k) \tag{12}$$

Where X^k is the value of X at iteration k of the ADMM algorithm.

The details of the update steps and stopping criteria for the ADMM algorithm are given in Algorithm 1,

Algorithm 1 NU-BGBM via ADMM

Input $\mathbf{Y},\mathbf{E},\mathbf{F},\mathbf{W}$

while $\frac{\|r^{k+1}\|_F}{\sqrt{3(MD+P)}} > \epsilon$ and $\frac{\|d^{k+1}\|_F}{\sqrt{3(MD+P)}} > \epsilon$ **do**

$\mathbf{A}^{(k+1)} \leftarrow [(\mathbf{WE})^T(\mathbf{WE})+\mu\mathbf{I}]^{-1}[(\mathbf{WE^T})\mathbf{W}(\mathbf{Y}-\mathbf{FB}^k-\mathbf{V}_1^k)+\mu(\mathbf{V}_2-\Lambda_2^k)]$;

$\mathbf{B}^{(k+1)} \leftarrow [(\mathbf{WF})^T(\mathbf{WF})+\mu\mathbf{I}]^{-1}[(\mathbf{WF^T})\mathbf{W}(\mathbf{Y}-\mathbf{EA}^k-\mathbf{V}_1^k)+\mu(\mathbf{V}_3-\Lambda_3^k)]$;

$\mathbf{S}^{(k+1)} \leftarrow \mathcal{S}_{\lambda/\mu}(\mathbf{V}_1^k-\Lambda_1^k)$;

$\mathbf{V}_1^{(k+1)} \leftarrow [(\mathbf{W})^T(\mathbf{W})+\mu\mathbf{I}]^{-1}[\mathbf{W^T W}(\mathbf{Y}-\mathbf{EA}^{k+1}-\mathbf{FB}^{k+1})+\mu(\mathbf{S}^{k+1}-\Lambda_3^k)]$

$\mathbf{V}_2^{(k+1)} \leftarrow \max(\mathbf{A}^{k+1}+\Lambda_2^{k+1},\mathbf{0})$

$\mathbf{V}_3^{(k+1)} \leftarrow \min(\max(\mathbf{B}^{k+1}+\Lambda_3^{k+1},\mathbf{0}),\mathbf{C})$

$\mathbf{\Lambda}_1^{(k+1)} \leftarrow \Lambda_1^k-(\mathbf{V}_1^{k+1}-\mathbf{S}^{k+1})$

$\mathbf{\Lambda}_2^{(k+1)} \leftarrow \Lambda_2^k-(\mathbf{V}_2^{k+1}-\mathbf{A}^{k+1})$

$\mathbf{\Lambda}_3^{(k+1)} \leftarrow \Lambda_3^k-(\mathbf{V}_3^{k+1}-\mathbf{B}^{k+1})$

$k = k+1$

end while

return $\mathbf{A}^{k+1},\mathbf{B}^{k+1},\mathbf{S}^{k+1}$

where $\mathcal{S}_{\lambda/\mu}(x) = \text{sign}(x)\max(x-\frac{\lambda}{\mu},0)$ is the element-wise soft shrinkage operator.

Data and Preprocessing

AVIRIS

In order to explore the use of the GBMM for extracting bathymetry, we acquired three hyperspectral scenes collected by NASA's Airborne Visible/Infrared Imaging Spectrometer (AVIRIS). AVIRIS measures radiance at 224 contiguous spectral bands between 400 and 2500nm, with bandwidths of approximately 10nm. The scenes were collected during the four day period of August 28th-31st, 2010 over southern Tampa Bay, Florida. We chose this region due to the presence of optically shallow water and the availability of groundtruth bathymetric lidar data. Additionally, this region presents complex bathymetric morphology due to the presence of barrier islands.

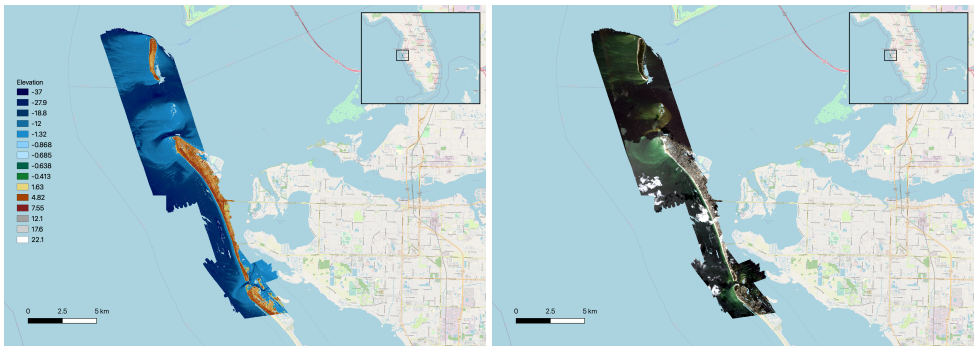

Figure 2: (**Left**) Bathymetry grid derived from bathymetric lidar data collected by NOAA's CHARTS system in November, 2010. Data were resampled to align with AVIRIS pixels. (**Right**) True color composite (bands: R=29,G=20,B=12) of median pixel values from 3 overlapping AVIRIS scenes collected August 29th, 30th, and 31st of 2010.

CHARTS

In addition to the AVIRIS hyperspectral imagery, we also acquired bathymetric lidar data for the same region. This data was collected by NOAA's Compact Airborne Rapid Total Survey (CHARTS) system, which integrates a 1 kHz, 532nm bathymetric lidar and a 9 kHz, 1064nm topographic lidar. This survey was conducted in early November, 2010.

Preprocessing

In order to compare the AVIRIS hyperspectral and NOAA CHARTS bathymetric lidar datasets, we conducted a few simple geospatial preprocessing steps using the open source QGIS software platform. First, due to the differences in spatial extent, we clipped the larger AVIRIS scenes to the extent of the smaller CHARTS survey. AVIRIS pixels outside the extent of the CHARTS survey were discarded because they did not have corresponding validation data. This also had the benefit of reducing the size of the AVIRIS datasets, which can be quite large due to the high number of spectral bands.

Next, in order to account for the difference in pixel size and centroid location between the CHARTS and AVIRIS data, we aligned the pixels of the CHARTS data to the AVIRIS scenes using the nearest neighbor resampling method. This allowed for a direct pixel-to-pixel comparison between the CHARTS and AVIRIS datasets.

These simple steps resulted in three spatially aligned AVIRIS scenes and one bathymetry grid. However, each of the three AVIRIS scenes contained significant cloud cover. In order to reduce this cloud contamination, we took the pixel-wise median value of corresponding bands from the three scenes in order to create a 224 band composite image. The pixel-wise median operation is a widely used method for reducing cloud contamination in satellite imagery. The resulting bathymetry grid and AVIRIS composite scene are shown in Figure 2.

USGS Spectral Library

In order to unmix the AVIRIS data, we assembled a spectral dictionary of independently measured material spectra from the United States Geological Survey (USGS) Spectral Library. The USGS Spectral Library contains thousands of spectral signatures from a wide range of material types, including minerals, soils, coatings, liquids, organic compounds, man-made materials, and vegetation. While future work may include added steps to algorithmically select the most appropriate spectra for unmixing a scene, due to the time contraints of this project, we selected six spectra from the larger library based on prior knowledge of the region of interest. The endmember materials selected were Water+Sediment, Coastal Water with Chlorophyl, Open Ocean, Dry Sand, Wet Sand, and Marsh Vegetation. The endmember spectra are shown in Figure 3.

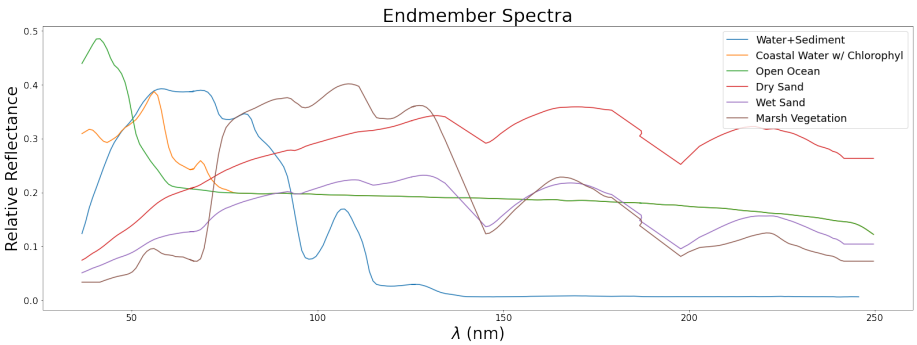

Figure 3: Endmember spectra acquired from USGS spectral library. Some spectra are an average of several similar spectral samples, such as multiple samples of sand and marsh vegetation.

Experiment

Using the ADMM solution for the NU-BGBM, we calculate the linear and bilinear abundance maps of the endmembers over the region of interest, as well as the sparse noise (artifact) maps. The input observation matrix $\mathbf{Y}$ was constructed by reshaping the AVIRIS composite image, while the input first and second order endmember dictionaries were constructed using the selected USGS spectra endmembers. The bandwise noise variance diagonal matrix $\mathbf{W}$ was calculated using the HySime algorithm. The details of this algorithm are outside the scope of this paper, however interested readers may refer to [3] for details on this algorithm. For the hyperparameters of the NU-BGBM, we used the suggested values $\mu = 0.01$ and $\epsilon = 10^{-6}$, with a maximum number of iterations of 100. As suggested by [1], we tested several values for λ, eventually selecting $\lambda = 1$ for the final model.

After calculating the abundance maps for the linear and nonlinear endmembers, we performed a pixel-wise linear regression between the abundances maps and the CHARTS bathymetry, excluding all missing values and values with elevations greater than 0 (i.e. dry land). This step was repeated three times, once with only the bilinear endmember abundances, once with only the linear endmember abundances, and once with both. Finally, we calculated the coefficients of determination (R^2) for the regressions and produced a map of the residuals between the predicted bathymetry and the true bathymetry, using the combined endmember regression output.

As a final step, we also implemented the DANSER algorithm, developed by [2], using the linear endmembers ($\mathbf{E}$). DANSER implements an ADMM based linear unmixing model, making it an appropriate comparison to NU-BGBM. We performed the same regression with the DANSER endmembers and compared the resulting R^2 with those from the NU-BGBM regressions.

3 Results

After running the NU-BGBM algorithm, which terminated after 25 iterations (by on the stopping criteria), we visualized both the 6 linear abundance maps and the 15 bilinear abundance maps. For brevity, we have included only the linear abundance maps in Figure 4, however the bilinear abundance maps as well as the DANSER abundance maps can be found in the additional file submitted along side this project.

Visual inspection of the abundance maps shows that highest abundances were found in the Open Ocean, Coastal Water, and Water+Sediment maps, while the lowest abundances were found in the Marsh Vegetation map. This makes sense given our prior knowledge of the region. However, there is also a clear and concerning spatial pattern between the maps. The spatial distribution of abundances appears to be very similar between all the maps, with the water endmembers dominating the entire scene. This does not fit with out expectation, especially given that there are areas in the region which should clearly be dominated by sand or marsh endmembers.

We also plotted the primal and dual residuals per algorithm iteration, which are shown in Figure 5. This plot showed that, while the dual problem converges to an optimum after 25 iterations, the primal problem appears to actually diverge. This may indicate an error with the algorithm implementation.

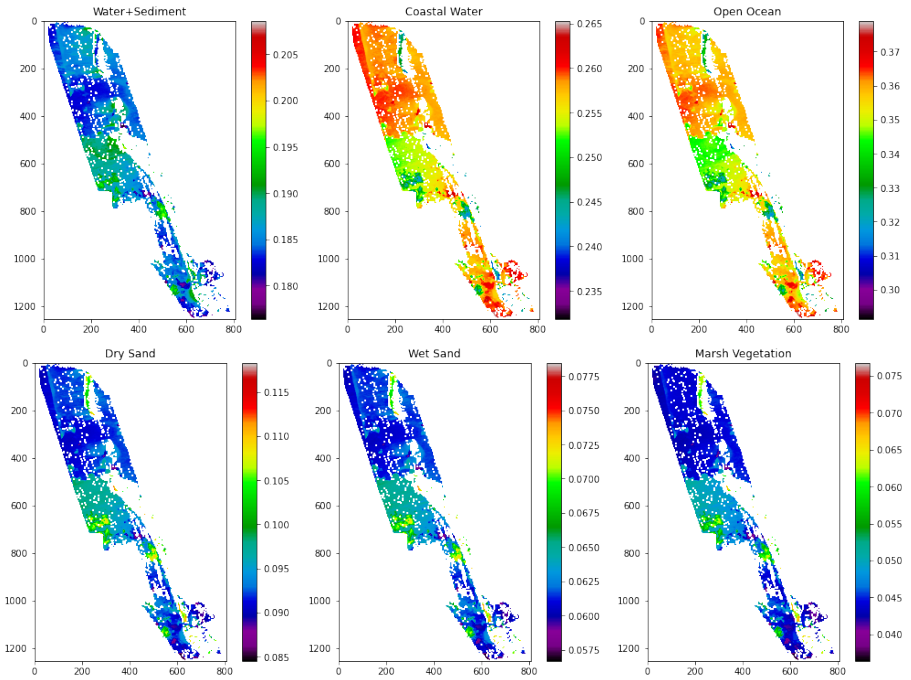

Figure 4: Relative abundance maps for the endmembers from the USGS spectral library.

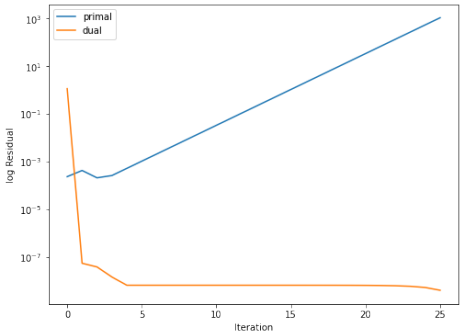

Figure 5: Primal and dual loss vs. algorithm iteration.

Finally, we performed a linear regression with the linear, bilinear, and combined abundance maps versus the bathymetry map. We also performed a purely linear unmixing using the DANSER algorithm and carried out the same type of regression. The coefficients of determination are shown in Table 1.

While none of these regressions were particularly successful compared to current SDB standards, the DANSER algorithm performed nearly 3 times better than the NU-BGBM with both endmember types. Interestingly, the NU-BGBM regression with only the bilinear endmembers performed nearly

Table 1: Coefficients of Determination

Endmembers	Algorithm	R^2
E	NU-BGBM	0.0893
F	NU-BGBM	0.1191
E and **F**	NU-BGBM	0.1265
E	DANSER	0.3659

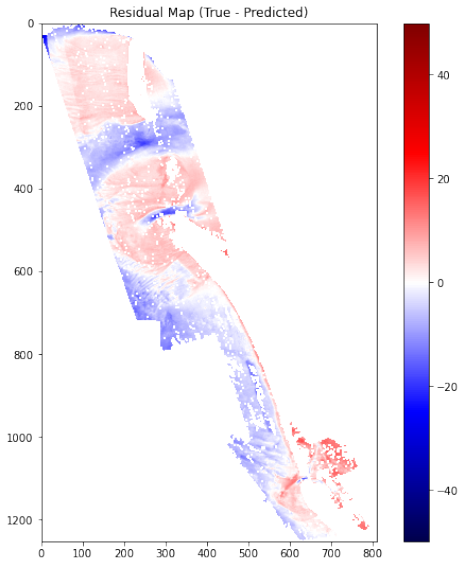

Figure 6: Linear Regression residuals for the $\mathbf{E}$ and $\mathbf{F}$ endmember regression. Values indicate measured - predicted bathymetry.

as well as the combined endmember regression, indicating that the bilinear model may still have potential to outperform the linear model for SDB regression.

Finally, we visualized the residuals between the combined endmember predicted bathymetry and the true bathymetry. The results are shown in Figure 6.

This map shows that the positive residuals are clustered in areas of shallower bathymetry, while the negative residuals cluster in deeper waters. This indicates that the variance of the predicted bathymetry was much smaller than the true variance.

4 Conclusions

We performed a bilinear spectral unmixing of an optically shallow coastal area in Tampa, FL and compared the results with groundtruth bathymetry via linear regression. While the results were unsatisfactory, the bilinear endmembers did have strong predictive power compared to the linear endmembers of the same model. However, the bilinear endmember significantly underperformed the linear endmembers of the DANSER algorithm. Visualizing a map of the predicted bathymetry indicated that the regression model dramatically under fit the measured data, producing a map with much lower variance than the true bathymetric map.

It is important to note that there are several potential sources of error that could have contributed to the unsatisfactory results. First, as noted in Figure 5, the primal loss diverges, indicating that there may be an error in the implementation of the NU-BGBM algorithm. Additionally, despite the preprocessing, there are still clear atmospheric effects and cloud contamination in the AVIRIS composite data set. Finally, significant changes in the bathymetric morphology due to storm activity during the one month period between the AVIRIS data collection and the CHARTS survey may have introduced error in the final regression.

In the future, we hope to find and correct any errors in the NU-BGBM algorithm implementation as well as test other nonlinear algorithms for spectral unmixing. After reconducting this experiment, hopefully with better results, we hope to use this work as part of a proposal to acquire atmospherically correct data from the DESIS sensor, a hyperspectral spectrometer currently operating on the International Space Station. Long term, we hope to perform a similar experiment using DESIS hyperspectral data and bathymetry data measured by ICESat-2's ATLAS spaceborne lidar. Additionally, we hope to test the efficacy of nonlinear spectral unmixing for simultaneous predicting bathymetry and K_d by comparing DESIS data with K_d measurements from NOAA's VIIRS satellite sensor.

References

[1] Li, C., Liu, Y., Cheng, J., Song, R., Peng, H., Chen, Q., & Chen, X. (2018). Hyperspectral Unmixing with Bandwise Generalized Bilinear Model. Remote Sensing, 10(10), 1600. https://doi.org/10.3390/rs10101600

[2] Fu, X., Ma, W.-K., Bioucas-Dias, J., & Chan, T.-H. (2016). Semiblind Hyperspectral Unmixing in the Presence of Spectral Library Mismatches. IEEE Transactions on Geoscience and Remote Sensing, 54(9), 5171–5184. https://doi.org/10.1109/TGRS.2016.2557340

[3] Bioucas-Dias, J. M., & Nascimento, J. M. P. (2008). Hyperspectral Subspace Identification. IEEE Transactions on Geoscience and Remote Sensing, 46(8), 2435–2445. https://doi.org/10.1109/TGRS.2008.918089

[4] Stumpf, R. P., Holderied, K., & Sinclair, M. (2003). Determination of water depth with high-resolution satellite imagery over variable bottom types. Limnology and Oceanography, 48(1part2), 547–556. https://doi.org/10.4319/lo.2003.48.1_part_2.0547